UNIVERSITY OF OKLAHOMA

GRADUATE COLLEGE

This is the thesis title

A DISSERTATION

SUBMITTED TO THE GRADUATE FACULTY

in partial fulfillment of the requirements for the

Degree of

DOCTOR OF PHILOSOPHY

By

YU-TING SHEN
Norman, Oklahoma
2017

This is the thesis title

A DISSERTATION APPROVED FOR THE
HOMER L. DODGE DEPARTMENT OF PHYSICS AND ASTRONOMY

BY

_____

Dr. Patrick Skubic, Chair

_____

Dr. Michael Strauss

_____

Dr. Ron Kantowski

_____

Dr. Deborah Watson

_____

Dr. S. Lakshmivarahan

'Blood, sweat & respect. First two you give, last one you earn."

- Dwayne Johnson

Acknowledgements

I would like to thank everyone who have helped me. Especially thanks to my advisors Patrick Skubic and Ximo Poveda Torres.

Contents

List of Tables

List of Figures

Abstract

Here is the abstract

Chapter 1

Introduction

Chapter 2

The Standard Model

This chapter outlines the theoretical and mathematical concepts of the high energy particle physics. The Standard Model of particle physics (SM) [10, 11, 12, 13, 14] is developed since the early 1970s and it has successfully explained almost all experimental results. The Standard Model is a well-tested and the most successful physics theory to describe the nature of the elementary particles and their interactions. An overview of the Standard Model is given in Section 2.1. After that, some of the open questions are mentioned in Section 2.2.

2.1 The Standard Model of Particle Physics

The Standard Model of particle physics is known as the most accurate theory for describing the elementary particles and the interactions between them. By combining the quantum mechanics and special relativity, the Standard Model is a relativistic *Quantum Field Theory* (QFT) based on a $SU(3)_C \otimes SU(2)_L \otimes U(1)_Y$ symmetry gauge group, where C denotes colour, L represents left chirality, and Y stands for weak hypercharge, respectively. The $SU(3)_C$ group is the basis for *Quantum Chromodynamics* (QCD) which describes the strong interaction and the $SU(2)_L \otimes U(1)_Y$ group is the foundation of the electroweak

interaction which unifies the electromagnetic and weak interactions. Therefore, the Standard Model Lagrangian is invariant under the local gauge transformation. According to *Noether's Theorem* [15], the invariance of an action of a physical system undergoes a symmetry transformation corresponding to a conservation law and vice versa. The gauge invariance of the Standard Model Lagrangian corresponds to the conserved quantum numbers, or the charges, of each interaction. The conserved charges are the three colour charge (red, blue, green) for the strong interaction, the third component of the weak isospin I_3 for the weak interaction, and the electric charge Q for the electromagnetic interaction.

2.1.1 Particle Content

According to the Standard Model, all matter around us is made of elementary particles called *quarks* and *leptons*. The quarks and leptons are called fermions which have half integral spin $s = \frac{1}{2}$, hence the fermions follow the Pauli exclusion principle which says no two fermions have the same quantum state at the same time. Each fermion has an anti-fermion with the equal mass but carries opposite electric charge, weak isospin and colour charge. There are six quarks and six leptons, they are grouped into three pairs, or "*generations*", ordered by their mass. The lightest and most stable particles constitute the first generation and they are constituents of ordinary matter. The heavier and less stable particles form the second and third generations and the heavier particles quickly decay to the next most stable particles. The three generations of quarks are up (u) and down (d), charm (c) and strange (s), and top (t) and bottom (b) quarks. The up-type quarks (u, c, t) carry $+\frac{2}{3}|e|$ charge and with isospin $+\frac{1}{2}$ while the down-type quarks (d, s, b) carry $-\frac{1}{3}|e|$ charge with isospin $-\frac{1}{2}$. The quarks carry an additional colour

charge of either red, green, or blue, and hence they only interact via the strong force. Because the strong force holds quarks together, only non-integer charges of the quark combinations are experimentally allowed. The quark combinations are called *hadrons* which can be categorised into *mesons* and *baryons*. The meson is composed by a quark and anti-quark pair ($q\bar{q}$) whereas the baryon is made up by three quarks (qqq or $\bar{q}\bar{q}\bar{q}$). Only colourless bound states of hadrons are allowed so the quark and anti-quark pair in a meson should contain colour and anti-colour and the three quarks in a baryon must carry different colours. The leptons are colourless and are therefore participating in the weak and electromagnetic force only. They do not participate in the strong interaction. The electron-type leptons (e, μ, τ) carry an elementary charge $|e|$ and their corresponding neutrinos (ν_e, ν_μ, ν_τ) are neutral. The neutrinos have very little mass and interact via weak force only. A summarised table of the properties of quarks and leptons is given in Table 2.1.

Generation	Fermion		particle	electric charge Q	weak isospin I_3	colour charge C	mass [GeV]
I	Quark	u	up quark	$+\frac{2}{3}|e|$	$+\frac{1}{2}$	r,g,b	0.0023
		d	down quark	$-\frac{1}{3}|e|$	$-\frac{1}{2}$	r,g,b	0.0048
	Lepton	e	electron	$-1|e|$	$-\frac{1}{2}$	-	0.00051
		ν_e	electron neutrino	0	$+\frac{1}{2}$	-	$< 2 \times 10^{-9}$
II	Quark	c	charm quark	$+\frac{2}{3}|e|$	$+\frac{1}{2}$	r,g,b	1.275
		s	strange quark	$-\frac{1}{3}|e|$	$-\frac{1}{2}$	r,g,b	0.095
	Lepton	μ	muon	$-1|e|$	$-\frac{1}{2}$	-	0.106
		ν_μ	muon neutrino	0	$+\frac{1}{2}$	-	$< 1.9 \times 10^{-7}$
III	Quark	t	top quark	$+\frac{2}{3}|e|$	$+\frac{1}{2}$	r,g,b	173.2
		b	bottom quark	$-\frac{1}{3}|e|$	$-\frac{1}{2}$	r,g,b	4.18
	Lepton	τ	tau	$-1|e|$	$-\frac{1}{2}$	-	1.777
		ν_τ	tau neutrino	0	$+\frac{1}{2}$	-	$< 1.82 \times 10^{-5}$

Table 2.1: The Standard Model fermions with charges and masses [1].

There are four fundamental forces in the universe: the strong force, the weak force, the electromagnetic force, and the gravitational force. The first three forces are described in the Standard Model, however, the gravitational force could not yet be included in the Standard Model. Because the effect of the gravitational force is very weak and can be negligible, the Standard Model works well without considering the gravitational force. Each force has a force-carrier particle called gauge boson and there is a quantum number associate to it. The gauge bosons of the strong force are eight massless *gluons*, g, which associate to colour charge C. The gauge bosons of the weak force are $W^{\pm}$ and Z^0 bosons which associate to weak isospin I_3. The gauge boson of the electromagnetic force is massless *photon*, γ, which associates to electric charge Q. Although the gluon and photon are massless particles, the $W^{\pm}$ and Z^0 bosons are massive. The mass of the $W^{\pm}$ and Z^0 bosons are $m_W = 80.385 \pm 0.015$ GeV and $m_Z = 91.1876 \pm 0.0021$ GeV [1], respectively. Table 2.2 shows the four fundamental forces, the relative strength and range together with the theories and the mediators.

Force	Rel. Strength	Range [m]	Theory	Mediator	Mass [GeV]
Strong	10	10^{-15}	Chromodynamics	Gluon	0
Weak	10^{-13}	10^{-18}	Flavourdynamics	$W^{\pm}$ and Z^0 bosons	80.4/91.2
Electromagnetic	10^{-2}	∞	Electrodynamics	Photon	0
Gravitational	10^{-42}	∞	General relativity	Graviton	-

Table 2.2: The four fundamental forces with the relative strength, interaction range, describing theory, and the mediator with its mass. The gravitational force is not a part of the Standard Model and the graviton is a theoretical particle.

2.1.2 Local Gauge Theory

The Lagrangian density of the Standard Model for the free fields[1] listed in the Equation 2.1 is invariant under local gauge transformation[2]

$$\mathcal{L} = \bar{\psi}(i\gamma^\mu \partial_\mu - m)\psi + e\bar{\psi}\gamma^\mu\psi \boldsymbol{A}_\mu - \frac{1}{4}\boldsymbol{F}_{\mu\nu}\boldsymbol{F}^{\mu\nu} \tag{2.1}$$

where $\boldsymbol{F}_{\mu\nu} = \partial_\mu \boldsymbol{A}_\nu - \partial_\nu \boldsymbol{A}_\mu$. The local gauge transformation means the scalar field ψ and the vector field $\boldsymbol{A}_\mu$ transform as

$$\psi(x) \rightarrow \psi'(x) = e^{i\theta(x)}\psi(x) \tag{2.2}$$

$$\boldsymbol{A}_\mu(x) \rightarrow \boldsymbol{A}'_\mu(x) = \boldsymbol{A}_\mu(x) + \frac{1}{e}\partial_\mu\theta(x). \tag{2.3}$$

By introducing the gauge term, i.e. the vector field, the interacting force can be obtained by calculating the derivatives of the *Euler-Lagrange equations*. The gauge field can be associated to particular spin one gauge bosons which mediate the force. The number of the mediating gauge bosons is equal to the dimension of the symmetry group. From the group theory, the dimension of an unitary group $U(n)$ is n^2 and the dimension of a special unitary group $SU(n)$ is $n^2 - 1$. Because the Standard Model is based on a $SU(3)_C \otimes SU(2)_L \otimes U(1)_Y$ symmetry gauge group, the number of mediators are 8 for $SU(3)_C$, 3 for $SU(2)_L$, and 1 for $U(1)_Y$ corresponding to 8 gluons for the strong interaction, 3 gauge bosons ($W^\pm$ and Z^0) for weak interaction, and 1 photon for the electromagnetic interaction.

---

[1]This is the Lagrangian density of QED. The three terms are fermion kinematic term, photon kinematic term, and interaction, respectively.

[2]In Dirac representation, the four contravariant gamma matrices are $\gamma^0 = \begin{pmatrix} 1 & 0 & 0 & 0 \\ 0 & 1 & 0 & 0 \\ 0 & 0 & -1 & 0 \\ 0 & 0 & 0 & -1 \end{pmatrix}$, $\gamma^1 = \begin{pmatrix} 0 & 0 & 0 & 1 \\ 0 & 0 & 1 & 0 \\ 0 & -1 & 0 & 0 \\ -1 & 0 & 0 & 0 \end{pmatrix}$, $\gamma^2 = \begin{pmatrix} 0 & 0 & 0 & -i \\ 0 & 0 & i & 0 \\ 0 & i & 0 & 0 \\ -i & 0 & 0 & 0 \end{pmatrix}$, $\gamma^3 = \begin{pmatrix} 0 & 0 & 1 & 0 \\ 0 & 0 & 0 & -1 \\ -1 & 0 & 0 & 0 \\ 0 & 1 & 0 & 0 \end{pmatrix}$

2.1.3   Strong interaction

The *Quantum Chromodynamics* (QCD) is the theory to describe the strong interaction. The gauge bosons are the eight massless gluons which carry three different colours (and anti-colours), red, green, and blue. Quarks interact with gluons hence they also carry colour charge C and can be represented in colour triplets

$$\psi = \begin{pmatrix} \psi_r \\ \psi_g \\ \psi_b \end{pmatrix}. \tag{2.4}$$

The QCD is based on the non-Abelian $SU(3)_C$ group which requires local gauge transformation

$$\psi \to \psi' = e^{ig_s\alpha_a(x)T^a}\psi \tag{2.5}$$

where the g_s is the strong coupling constant, $\alpha_a(x)$ are arbitrary functions of space-time, and T^a are the generators of the non-Abelian $SU(3)_C$ group and the summation over a with $a = 1,\ldots,8$ is implied. The Lagrangian density is invariant under the local gauge transformation by introducing the new form of the gauge fields and the covariant derivative

$$\boldsymbol{G}_\mu^a \to \boldsymbol{G}_\mu^a - \partial_\mu\alpha^a(x) - g_s f_{abc}\alpha^b(x)\boldsymbol{G}_\mu^c \tag{2.6}$$

$$\partial_\mu \to D_\mu = \partial_\mu + ig_s T_a \boldsymbol{G}_\mu^a \tag{2.7}$$

where f_{abc} is the structure constant. The Lagrangian density of QCD is given by

$$\mathcal{L}_{QCD} = \bar{\psi}(i\gamma^\mu\partial_\mu - m)\psi - g_s(\bar{\psi}\gamma^\mu T_a\psi)\boldsymbol{G}_\mu^a - \frac{1}{4}\boldsymbol{G}_{\mu\nu}^a\boldsymbol{G}_a^{\mu\nu} \tag{2.8}$$

where the field strength tensor $\boldsymbol{G}_{\mu\nu}^a = \partial_\mu\boldsymbol{G}_\nu^a - \partial_\nu\boldsymbol{G}_\mu^a - g_s f_{abc}\boldsymbol{G}_\mu^b\boldsymbol{G}_\nu^c$ causing self-interactions between the gluons. The strong force increases with distance between quarks, therefore, the quarks exist only as colourless compounds such as meson or baryon mentioned in

Section 2.1.1. The production of a single quark is accompanied by the creation of an anti-quark from vacuum to form a quark and anti-quark pair as a colourless compound. This is called *hadronisation*. The phenomena that confined quarks in the small interaction range is called *confinement*. But at small distance or high energy, the quarks can be considered as quasi-free particles. This is referred to as *asymptotic freedom*.

2.1.4 Electroweak interaction

Fermi formulated the first weak interaction theory in 1933 [16], however, the theory only holds for energies less than 100 GeV. Glashow, Salam, and Weinberg (GSW) proposed a new model [10, 12, 11] which unifies electromagnetic and weak forces to become *electroweak* (EW) force and this new *GSW model* can apply to the energy greater than 100 GeV. The electroweak theory is based on $SU(2)_L \otimes U(1)_Y$ gauge symmetry where the subscripts L denotes the left-handedness because only the left-handed fermions (and right-handed anti-fermions) and Y denotes the weak hypercharge, a new quantum number, which relates to the electric charge Q and the weak isospin I_3 by the *Gell-Mann-Nishijima relation* [17, 18]

$$Y = 2(Q - I_3). \tag{2.9}$$

The left-handed and right-handed fermion field ψ can be decomposed into two components

$$\psi = P_L\psi + P_R\psi \tag{2.10}$$

$$= \psi_L + \psi_R \tag{2.11}$$

where the projection operators P_L and P_R are defined as[3]

$$P_L = \frac{1}{2}(1 - \gamma^5) \tag{2.12}$$

$$P_R = \frac{1}{2}(1 + \gamma^5). \tag{2.13}$$

The projection operators satisfy $P_L P_R = 0$ and $P_L + P_R = 1$. Experimental observations show the right-handed neutrinos don't participate in all the interactions described in the Standard Model so the ψ_R is a singlet and $I_3 = 0$[4]. The local gauge transformations of the $SU(2)_L \otimes U(1)_Y$ are

$$\psi_L \rightarrow \psi'_L = e^{i\alpha_a(x)T^a} e^{i\beta(x)Y} \psi_L \tag{2.14}$$

$$\psi_R \rightarrow \psi'_R = e^{i\beta(x)Y} \psi_R \tag{2.15}$$

where $T^a = \frac{\sigma^a}{2}$ are the generators of $SU(2)_L$ with Pauli matrix σ^a[5] and Y is the generator of $U(1)_Y$. The $\alpha_a(x)$ and $\beta(x)$ depend on the space-time. The covariant derivative with respect to the $SU(2)_L \otimes U(1)_Y$ is

$$D_\mu = \partial_\mu + ig_W T_a \boldsymbol{W}^a_\mu + ig_Y Y \boldsymbol{B}_\mu \tag{2.16}$$

where g_W and g_Y are coupling constants and $\boldsymbol{W}^a_\mu$ ($a = 1, 2, 3$) and $\boldsymbol{B}_\mu$ are the gauge fields. The gauge fields $\boldsymbol{W}^a_\mu$ and $\boldsymbol{B}_\mu$ transform under the $SU(2)_L \otimes U(1)_Y$ symmetry as

$$\boldsymbol{W}^a_\mu \rightarrow \boldsymbol{W}^a_\mu - \frac{1}{g_W}\partial_\mu \alpha^a(x) - \epsilon^{abc}\alpha^b(x)\boldsymbol{W}^c_\mu \tag{2.17}$$

$$\boldsymbol{B}_\mu \rightarrow \boldsymbol{B}_\mu - \frac{1}{g_Y}\partial_\mu \beta(x) \tag{2.18}$$

where ϵ^{abc} is the Levi-Civita tensor. The Lagrangian density of the electroweak is given by

$$\mathcal{L}_{EW} = \bar{\psi}_L(i\gamma^\mu D_\mu - m)\psi_L + \bar{\psi}_R(i\gamma^\mu D_\mu - m)\psi_R - \frac{1}{4}\boldsymbol{W}^a_{\mu\nu}\boldsymbol{W}^{\mu\nu}_a - \frac{1}{4}\boldsymbol{B}_{\mu\nu}\boldsymbol{B}^{\mu\nu} \tag{2.19}$$

---

[3]γ^5 is the product of the four gamma matrices. $\gamma^5 = i\gamma^0\gamma^1\gamma^2\gamma^3 = \begin{pmatrix} 0 & 0 & 1 & 0 \\ 0 & 0 & 0 & 1 \\ 1 & 0 & 0 & 0 \\ 0 & 1 & 0 & 0 \end{pmatrix}$

[4]The left-handed fermion state ψ_L is a doublet.

[5]The Pauli matrices are $\sigma_1 = \begin{pmatrix} 0 & 1 \\ 1 & 0 \end{pmatrix}$, $\sigma_2 = \begin{pmatrix} 0 & -i \\ i & 0 \end{pmatrix}$, and $\sigma_3 = \begin{pmatrix} 1 & 0 \\ 0 & -1 \end{pmatrix}$

where $\boldsymbol{W}_{\mu\nu}^a$ and $\boldsymbol{B}_{\mu\nu}$ are the field strength tensors

$$\boldsymbol{W}_{\mu\nu}^a = \partial_\mu \boldsymbol{W}_\nu^a - \partial_\nu \boldsymbol{W}_\mu^a - g_W \epsilon^{abc} \boldsymbol{W}_\mu^b \boldsymbol{W}_\nu^c \tag{2.20}$$

$$\boldsymbol{B}_{\mu\nu} = \partial_\mu \boldsymbol{B}_\nu - \partial_\nu \boldsymbol{B}_\mu \tag{2.21}$$

and $\bar{\psi} \equiv \psi^\dagger \gamma^0$ is the adjoint spinor of ψ[6]. Therefore, the mass eigenstates are the mixture of the gauge fields

$$\boldsymbol{W}_\mu^\pm = \frac{1}{\sqrt{2}}(\boldsymbol{W}_\mu^1 \mp i\boldsymbol{W}_\mu^2) \tag{2.22}$$

$$\begin{pmatrix} \boldsymbol{A}_\mu \\ \boldsymbol{Z}_\mu \end{pmatrix} = \begin{pmatrix} \cos\theta_W & \sin\theta_W \\ -\sin\theta_W & \cos\theta_W \end{pmatrix} \begin{pmatrix} \boldsymbol{B}_\mu \\ \boldsymbol{W}_\mu^3 \end{pmatrix}. \tag{2.23}$$

Thus, the mass eigenstates $\boldsymbol{A}_\mu$, $\boldsymbol{W}_\mu^\pm$, and $\boldsymbol{Z}_\mu$ are identified as the photon, γ, $W^\pm$ and Z^0 bosons experimentally. The *Weinberg weak mixing angle* θ_W is defined as

$$\tan\theta_W = \frac{g_Y}{g_W}. \tag{2.24}$$

The coupling constants g_W and g_Y are related to the electric charge by

$$e = g_W \sin\theta_W = g_Y \cos\theta_Y. \tag{2.25}$$

And the weak eigenstates of quark, q', are the linear combinations of the mass eigenstates of quark, q, by the *Cabbibo-Kobayashi-Maskawa* (CKM) matrix [19]

$$\begin{pmatrix} d' \\ s' \\ b' \end{pmatrix} = \begin{pmatrix} V_{ud} & V_{us} & V_{ub} \\ V_{cd} & V_{cs} & V_{cb} \\ V_{td} & V_{ts} & V_{tb} \end{pmatrix} \begin{pmatrix} d \\ s \\ b \end{pmatrix}. \tag{2.26}$$

The CKM matrix allows the quarks changing their flavour and generation as observed in the experiment. Similarly, the *Pontecorvo-Maki-Nakagawa-Sakata* (PMNS) matrix [20] is responsible for the flavour changing of the neutrinos.

---

[6] $\psi^\dagger$ is the hermitian conjugate of ψ

Spontaneous symmetry breaking and Higgs mechanism

The gauge bosons of the weak interaction, $W^\pm$ and Z^0, are massive particles[7]. However, the existence of the mass terms violate the gauge invariance of the $\mathcal{L}_{EW}$. In order to explain the mass of gauge bosons, the Englert-Brout-Higgs mechanism [21, 22, 23, 24, 25] was proposed in 1964. A new scalar complex $SU(2)_L$ doublet field Φ is introduced in the Higgs mechanism

$$\Phi = \begin{pmatrix} \Phi^+ \\ \Phi^0 \end{pmatrix} = \begin{pmatrix} \Phi_1 & i\Phi_2 \\ \Phi_3 & i\Phi_4 \end{pmatrix} \tag{2.27}$$

with hypercharge $Y = 1$ and four degrees of freedom, Φ_i, which are scalar fields and called the *Goldstone modes*. The Lagrangian density for this new field, Higgs field, is

$$\mathcal{L}_\Phi = (D^\mu \Phi)^\dagger (D_\mu \Phi) - V(\Phi) \tag{2.28}$$

where the Higgs potential is defined as

$$V(\Phi) = \mu^2 |\Phi|^2 + \lambda |\Phi|^4 \tag{2.29}$$

where μ and λ are free parameters. The Higgs potential is shown in Figure 2.1. The Higgs potential is the rotation $U(1)$ symmetry. Choosing any of the points at the bottom of the Higgs potential breaks the symmetry spontaneously. The *spontaneously symmetry breaking* (SSB) means the Lagrangian keeps invariant under certain symmetry but no longer invariant at the ground state.

Because the Higgs potential is invariant under $SU(2)_L \otimes U(1)_Y$, the parameters μ and λ must satisfy $\mu^2 < 0$ and $\lambda > 0$ resulting in a set of degenerate ground states where $\langle 0|\Phi|0\rangle \neq 0$. Among the degenerate ground states, the ground state is often chosen to

---

[7]$m_W = 80.385 \pm 0.015$ GeV and $m_Z = 91.1876 \pm 0.0021$ GeV
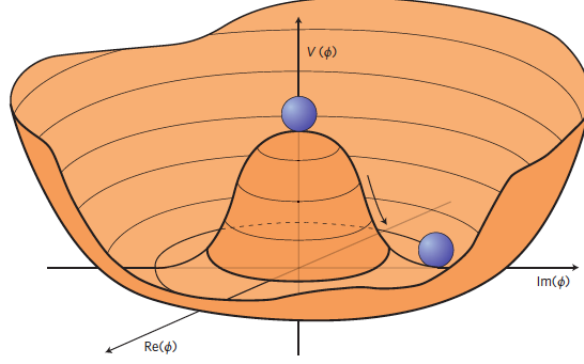
Figure 2.1: An illustration of the Higgs potential which has the form of a Mexican hat. The figure is taken from [3].

have the form

$$\Phi = \frac{1}{\sqrt{2}} \begin{pmatrix} 0 \\ v \end{pmatrix} \tag{2.30}$$

where $v = \sqrt{-\mu^2/\lambda}$ is the *the vacuum expectation value* (VEV). This particular choice of the ground state breaks the $SU(2)_L \otimes U(1)_Y$ symmetries spontaneously and ensures the unbroken electromagnetic interaction under $U(1)_{EM}$ symmetry and photon being massless. By introducing a massive particle, Higgs boson H, the Higgs field can be re-written as

$$\Phi = \frac{1}{\sqrt{2}} \begin{pmatrix} 0 \\ v + H \end{pmatrix} \tag{2.31}$$

and the kinematic term of the Lagrangian density becomes

$$\mathcal{L}_{\Phi}^{\text{kinematic}} = (D^\mu \Phi)^\dagger (D_\mu \Phi) \tag{2.32}$$

$$= \frac{1}{2} \partial_\mu H \partial^\mu H + (v + H)^2 \left\{ \frac{g_W^2}{4} \boldsymbol{W}_\mu^\dagger \boldsymbol{W}^\mu + \frac{g_W^2}{8\cos^2\theta_W} \boldsymbol{Z}_\mu^\dagger \boldsymbol{Z}^\mu \right\} \tag{2.33}$$

and the Higgs potential is now

$$V(\Phi) = -\frac{v^2 \lambda}{2} (v + H)^2 + \frac{\lambda}{4} (v + H)^4. \tag{2.34}$$

Thus the masses of the $W^\pm$ and Z^0 are obtained by the interaction between the gauge

12

bosons and Higgs boson. The masses are defined as

$$m_H = v\sqrt{2\lambda}, \quad m_W = \frac{v}{2}g_W, \quad m_Z = \frac{v}{2}\sqrt{g_W^2 + g_Y^2}, \quad m_\gamma = 0. \tag{2.35}$$

However, the masses of fermions are obtained by the *Yukawa interaction*

$$\mathcal{L}_{\text{Yukawa}} = y_f \bar{L}_L \Phi f_R + y_f \bar{Q}_L \Phi f_R + \text{h.c.} \tag{2.36}$$

where the y_f is *Yukawa coupling*, f stands for $\{\ell^i, u^i, d'^i\}$ and h.c. represents the hermitian conjugate, respectively. The $\bar{L}_L$ and $\bar{Q}_L$ are the left-handed lepton and quark doublet and f_R is the lepton or quark singlet. The mass of fermion is defined as

$$m_f = \frac{v}{\sqrt{2}} y_f \tag{2.37}$$

where y_f is a free parameter which causes the fermion mass not predictable. Finally, the non-zero VEV, v, can be related to *Fermi constant*, G_F, by

$$v = \frac{1}{\sqrt{\sqrt{2}G_F}} \approx 246 \text{ GeV.} \tag{2.38}$$

2.1.5 The discovery of Higgs boson

A lot of the Standard Model predictions are successfully confirmed by the experimental observations besides the existence of the theoretical Higgs boson. The search of the Higgs boson has become a major goal of the experimental particle physicists. A Higgs-like resonance was discovered and announced on July 4th 2012 by the ATLAS[8] and CMS[9] collaborations [4, 5]. By combining the data with integrated luminosities of 4.8 fb^{-1} collected at $\sqrt{s} = 7$ TeV in 2011 and 5.8 fb^{-1} at $\sqrt{s} = 8$ TeV in 2012, the ATLAS experiment measured the mass of the Higgs boson to be 126.0 ± 0.4 (stat.) ± 0.4 (syst.) GeV with significance of 5.9σ corresponding to a background fluctuation

---

[8]A Toroidal LHC ApparatuS
[9]Compact Muon Solenoid

probability of 1.7×10^{-9} [4]. In the meantime, the CMS experiment announced the mass of the Higgs boson to be 125.3 ± 0.4 (stat) ± 0.5 (syst.) GeV with significance 5.0σ using integrated luminosities of up to 5.1 fb^{-1} at 7 TeV and 5.3 fb^{-1} at 8 TeV [5]. The $H \rightarrow ZZ^{(*)} \rightarrow 4\ell$, $H \rightarrow \gamma\gamma$, and $H \rightarrow WW^{(*)} \rightarrow e\nu\mu\nu$ channels were studied by the ATLAS collaboration and the $H \rightarrow \gamma\gamma, ZZ, W^+W^-, \tau^+\tau^-$, and $b\bar{b}$ channels were studied by the CMS collaboration. In the Figure 2.2 shows the local p-value as a function of the Higgs mass for ATLAS and CMS results, respectively.

(a) ATLAS results   (b) CMS results
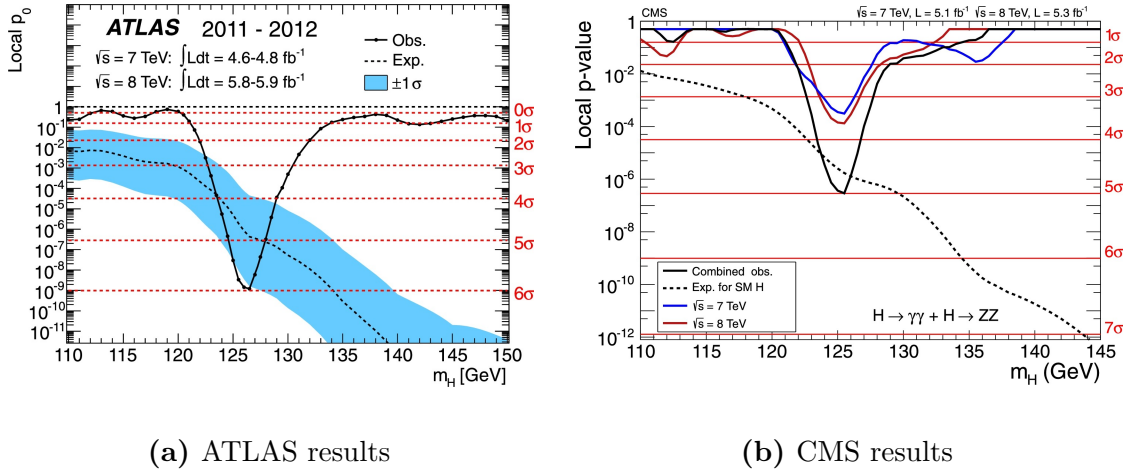
Figure 2.2: The observed local p-value as a function of m_H for the ATLAS [4] and CMS [5] experiment, respectively. The dashed line shows the expected local p_0 for a Standard Model Higgs boson. The horizontal lines denotes the p-values corresponding to significances of 1 to 6σ.

2.2   Beyond the Standard Model

Although the Standard Model is an incredible successful theory for explaining the phenomenon in the particle physics, it leaves some questions which can no be answered. Some of the unanswered questions are introduced in the rest part of this section.

2.2.1 Hierarchy problem

The weakest force in the Standard Model is the weak force but the strength of the weak force is 10^{24} times as strong as gravitational force which doesn't incorporate into the Standard Model. The large discrepancy between the weak force and the gravitational force is called the hierarchy problem [26, 27, 28]. The classical potential of the Standard Model Higgs field Φ is

$$V(\Phi) = \mu^2 |\Phi|^2 + \lambda |\Phi|^4. \tag{2.39}$$

Since the Standard Model requires the *vacuum expectation value* (VEV) for Φ, $\langle \Phi \rangle$, at the minimum of the potential non-vanishing, this only satisfied if $\mu^2 < 0$ and $\lambda > 0$. However, the parameter μ^2 receives enormous radiative corrections causing it ultraviolet divergent as shown in Equation 2.40.

$$\mu^2 = \mu_{bare}^2 - \frac{|\lambda_f|^2}{8\pi} \Lambda_{UV}^2 + \mathcal{O}(\Lambda_{UV}^2) \tag{2.40}$$

where μ_{bare} is the Higgs mass, $-\frac{|\lambda_f|^2}{8\pi} \Lambda_{UV}^2$ is the one-loop correction, and Λ_{UV} is an ultraviolet momentum cutoff which is valid up to the Plank scale 10^{19} GeV. The electroweak gauge bosons $W^\pm$ and Z^0 obtain their finite masses from $\langle \Phi \rangle$ so the μ^2 cannot be divergent. There must some unknown mechanism to protect from divergence.

2.2.2 Dark matter and dark energy

The matters we know today compose of only 5% [29, 30] of the content of the universe and the remaining part is something we don't know. This unknown matter is called *Dark Matter* (DM) [31] which makes up about 27% of the universe and the rest 68% are called *Dark Energy* (DE) [29, 30]. Because dark matter interacts weakly and doesn't interact with the electromagnetic force, it doesn't absorb, emit, or reflect light causing it

hard to detect directly. The name dark matter comes from it is invisible. Dark energy distributes evenly in both space and time throughout the universe so it doesn't dilute when the universe expands. The observed scientific data hints the presence of dark energy is necessary to explain the accelerated expansion of the universe.

2.2.3 Grand Unification

Maxwell unified the electricity and magnetism into electromagnetism in the 1860s. About a century later, physicists successfully developed theory of electroweak which links the electromagnetism and the weak force. Because of the triumph of electroweak theory, theorists raise the question of the possibility to unify all forces. The *Grand Unified Theory* (GUT) [32], which tries to link three of the four known forces together, is developed in the mid-1970s by theorists The GUT proposes that the electromagnetic force, weak force, and strong force unify to one force at the GUT scale, $\Lambda_{GUT} \approx 10^{16}$ GeV. So the three running coupling constants [33] are expected to be converged at the GUT scale. However, the current experiment results show the coupling constants still different as shown in Figure 2.3.

2.2.4 More questions

There are some more interesting questions which we don't know the answers. For example, we don't know the reason why there are 61 elementary particles and more than 20 arbitrary parameters in the Standard Model. Also, the Standard Model doesn't explain why there are only three generations. The amount of matter and anti-matter are equal at the beginning of the universe based on the prediction of the Standard Model but the matter dominates in the currently universe which the Standard Model couldn't answer the reason
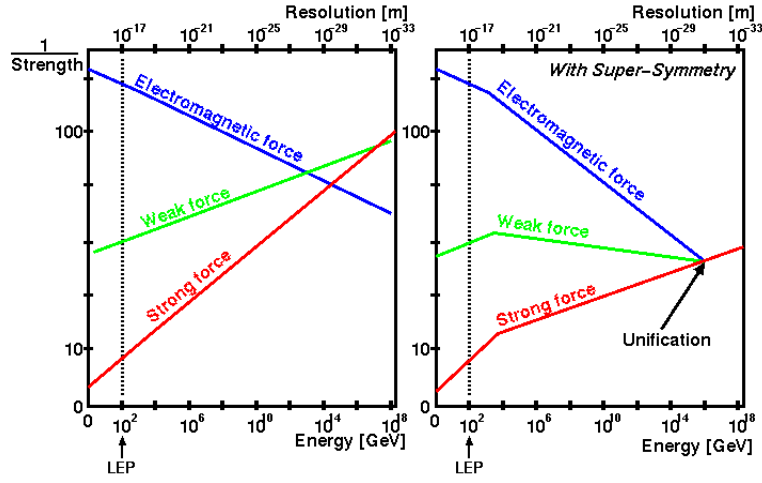
Figure 2.3: The measured running coupling constants in the Standard Model (left) and prediction in the GUT (right). The three lines show the inverse value of the coupling constant for the three fundamental forces. This figure is taken from [6].

why.

In order to answer these questions, there are many theories being developed on the top of Standard Model but none of them has been observed. One of the most probable candidate for answering these question is supersymmetry which will be introduced in the next chapter.

Chapter 3

Suppersymmetry

Chapter 4

The ATLAS Experiment at LHC

The European Organisation for Nuclear Research (CERN[1]) was founded in 1954 and is based in the suburb of Geneva on the Franco–Swiss border. The main function of CERN is to provide particle accelerators and detectors for high-energy physics research. The physicists and engineers at CERN are probing the fundamental structure of the universe using the world's largest and most complex scientific facility — the *Large Hadron Collider* (LHC) [34]. In the LHC, the particles are boosted to high energies and collide at close to the speed of light. The results of the collisions are recorded by the various detectors. There are seven experiments at the LHC. The biggest of these experiments are *ATLAS* (A Toroidal LHC ApparatuS) [2] and *CMS* (Compact Muon Solenoid) [35] which use general-purpose detectors to investigate a broad physics programme ranging from the search for the Higgs boson to extra dimensions and particles that could make up dark matter. The *ALICE* (A Large Ion Collider Experiment) [36] experiment is designed to study the physics of quark-gluon plasma form and the *LHCb* (Large Hadron Collider beauty) [37] experiment specialises in investigating of CP violation[2] by studying the

---

[1]The name CERN is derived from the acronym for the French Conseil Européen pour la Recherch Nucléaire

[2]The CP violation is violation of the charge conjugate and parity symmetry which says if a particle is interchanged with its anti-particle and its spatial coordinates are inverted, then the physics laws should be the same.

b-quark. These four detectors sit underground in huge caverns of the LHC ring. The rest three experiments, *TOTEM* [38], *LHCf* [39], and *MoEDAL* [40], are smaller. The TOTEM (TOTal Elastic and diffractive cross section Measurement) [38] experiment aims at the measurement of total cross section, elastic scattering, and diffractive dissociation. The LHCf (Large Hadron Collider forward) [39] experiment is intended to measure the neutral particle produced by the collider using the forward particles. The prime motivation of the MoEDAL (Monopole and Exotics Detector at the LHC) [40] experiment is to search directly for the magnetic monopole. An overview of the LHC is described in Section 4.1 and the detector apparatus of the ATLAS experiment is outlined in Section 4.2.

4.1 The Large Hadron Collide

The LHC [34] is the world's largest and most powerful accelerator which accelerates and collides protons in a 26.7 km circumference crossing the Franco–Swiss border 100 m underground. Built in the tunnel of the former *LEP* (Large Electron–Positron), the LHC is capable of colliding protons as well as heavy ions. Comparing with the LEP which collides electrons and positrons, the advantage of the LHC is the lower energy loss[3] in the synchrotron radiation, such that higher energies can be reached by the LHC. The LHC is designed for collisions at a centre-of-mass energy $\sqrt{s} = 14$ TeV and an instantaneous luminosity of $\mathcal{L} = 10^{34}$ cm^{-2}s^{-1}. Figure 4.1 shows the infrastructure of the LHC and the pre-accelerator system.

The protons are extracted by ionisation from a hydrogen source and are accelerated to 50 MeV by the linear accelerator *LINAC2*. Then they are injected into the *Proton Synchrotron Booster* (PSB) where the proton energies are increased to 1.4 GeV before they

---

[3]The energy loss for protons is about eleven orders of magnitude smaller than the electrons
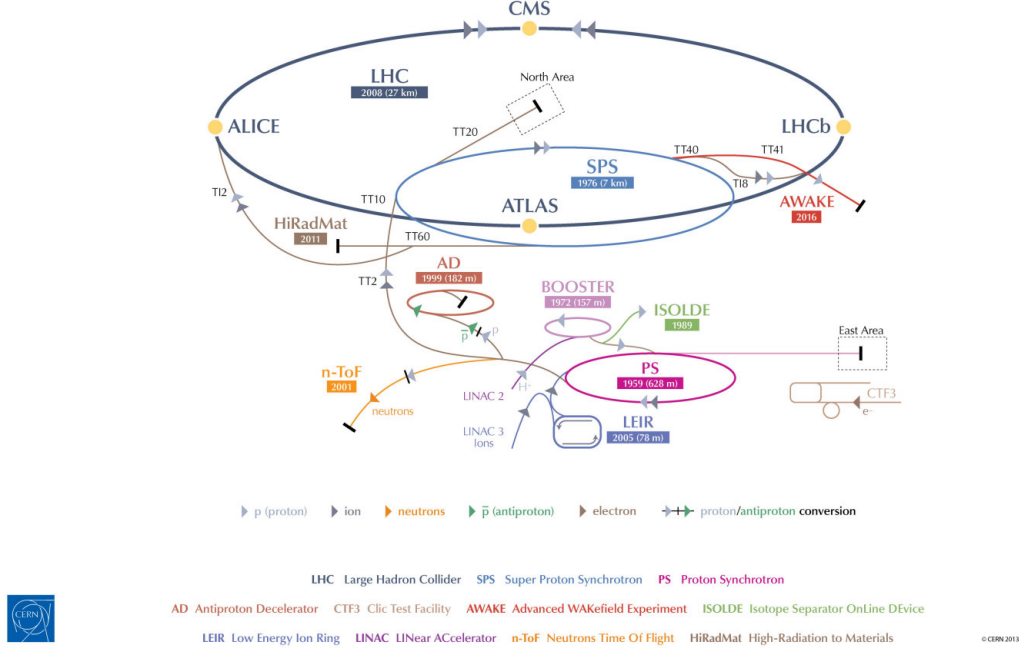
Figure 4.1: The accelerator complex at CERN [7].

enter the *Proton Synchrotron* (PS) which accelerates the protons to 25 GeV. Next, the proton energies are increasing to 450 GeV in the *Super Proton Synchrotron* (SPS). Finally, the protons are split into two beams and enter the LHC where the two beams run in two adjacent beam pipes with opposite directions. In order to keep the protons on the circular trajectory in the LHC, 1232 superconducting dipole magnets [41] generate a magnetic field strength of 8.33 T to bend the proton beams in eight arcs. Additionally, 392 quadrupole magnets [41] are installed to focus the beam. A cryogenic system running with super-fluid helium-4 is used to cool down the superconducting magnets to a temperature of 1.7 K.

For a given physics process, the event rate is proportional to the cross section σ of this process.

$$\frac{dN}{dt} = \mathcal{L} \cdot \sigma \tag{4.1}$$

where N is the number of events and $\mathcal{L}$ denotes the luminosity of the beam. The luminosity

of the beam, $\mathcal{L}$, can be calculated by

$$\mathcal{L} = \frac{N^2 f}{4\pi \sigma_x \sigma_y} \cdot F \tag{4.2}$$

where N is the number of protons, f is the bunches crossing frequency, and the σ_x and σ_y are the x and y components for cross section σ. The geometric luminosity reduction factor, F, is related to the crossing angle at the *interaction point* (IP). Considering a beam consisting of 1.15×10^{11} protons with bunching spacing of 25 ns, the transversal size of the bunch at IP 16×10^{-4} cm, and taking the geometric luminosity reduction factor as 1, the design luminosity of 10^{34} cm^{-2}s^{-1} can be reached.

The first beam was circulated through the collider on the morning of 10 September 2008 [42]. However, a magnet quench incident occurred on 19 September 2008 and caused extensive damage to over 50 superconducting magnets, their mountings, and the vacuum pipe. Most of 2009 was spent on repairs the damage caused by the magnet quench incident and the operations resumed on 20 November of that year. The first phase of data-taking (Run 1) started at the end of 2009 and the beam energy was increased to a centre-of-mass $\sqrt{s} = 7$ TeV in 2011 and $\sqrt{s} = 8$ TeV in 2012. The total integrated luminosity of 5.46 fb^{-1} was collected in 2011 and of 22.8 fb^{-1} was collected in 2012. Since 13 February 2013 the LHC was in the Long Shutdown 1 (LS1) phase for maintenance and upgrades. On 5 April 2015, the LHC restarted and was operating at a centre-of-mass energy $\sqrt{s} = 13$ TeV throughout the Run 2 phase[4].

---

[4]The Run 2 data-taking started from 2015

4.2 The ATLAS experiment

The ATLAS[5] detector [2] is a multi-purpose detector housed in its cavern at point 1 at the LHC [34]. It is the largest experiment at the LHC with a length of 44 m, a diameter of 25 m, and a weight of approximately 7000 tonnes. It consists of three high precision sub-detector systems which are arranged concentrically around the interaction point and in forward and backward symmetrically. Related to this symmetry, the ATLAS detector is sectioned into the central barrel region with one end-cap region perpendicular to the beam pipe on either side. Figure 4.2 shows an overview of the ATLAS detector with its major components.
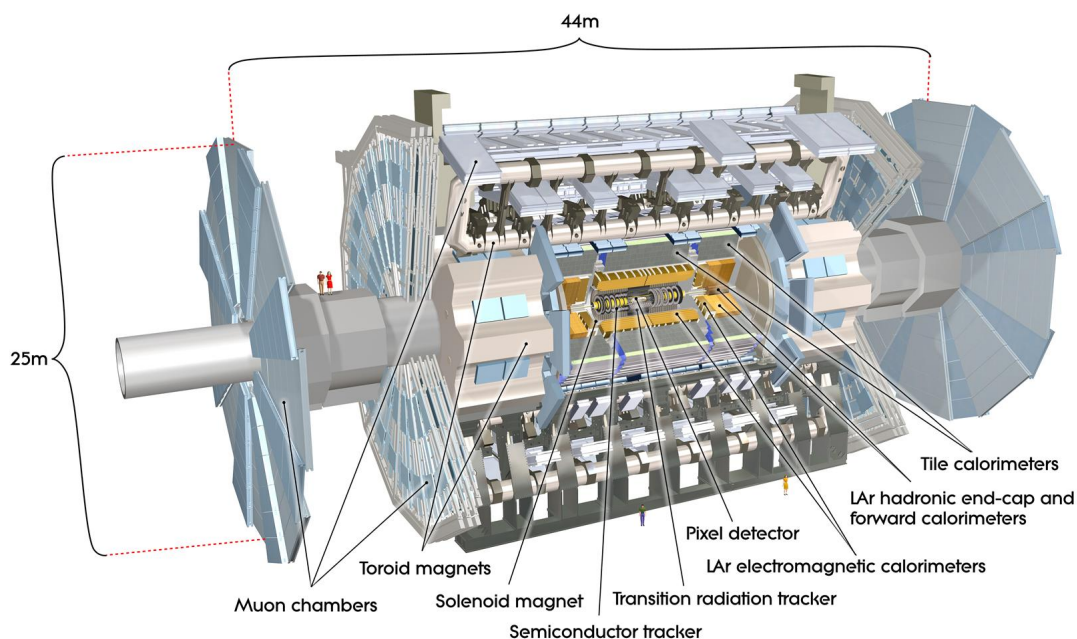
Figure 4.2: Overview of the ATLAS detector [2].

The ATLAS detector is designed to record the proton-proton interactions delivered by the LHC. It can identify particles and measure their tracks and energies with very high precision, therefore, it is sensitive to large areas of particle physics phenomena

---

[5]A Toroidal LHC Apparatus

from the precision measurement of the Standard Model to beyond the Standard Model (BSM). The detector is constituted by three sub-detector systems and the magnet system. The innermost part of the detector is called the *inner detector* which identifies and reconstructs the charged particles as well as the primary and secondary vertices. Around it, the *calorimeter* system is built as a cylindrical barrel with caps at each end to measure the particle energies. The detector is completed by the *muon spectrometer* which performs identification and measurement of momenta of muons. The magnetic system produces a field of $B = 0.5$ T and $B = 1$ T at barrel and two end-cap, respectively. The detector has to withstand large collision rates with approximately 1000 particles per collision, therefore, a fast readout and a three-level trigger system are implemented to reduce the event rate from 40 MHz to 200 Hz. The ATLAS coordinate system and the detail of each sub-detector systems are described in the following sections.

4.2.1 The ATLAS coordinate system

ATLAS uses a *right-handed coordinate system* with its origin at the nominal proton-proton interaction point (IP) in the centre of the detector and the z-axis along the beam pipe. Along the z-axis the detector is divided into side-A (positive z) and side-C (negative z). The positive x-axis is defined by the direction pointing from the interaction point to the centre of the LHC ring, and the positive y-axis points upward.The azimuthal angle ϕ is measured around the beam pipe and the polar angle θ is the angle from the z-axis. The transverse momentum p_T, the transverse energy E_T and the missing transverse energy E_T^{miss} are defined in the transverse plane[6], here exemplary for p_T:

$$p_T = \sqrt{p_x^2 + p_y^2} \tag{4.3}$$

---

[6] $x - y$ plane

An important quantity in hadron collider physics is the *rapidity*, y, because of the invariance y under Lorentz boosts in the longitudinal direction. The rapidity is defined as

$$y = \frac{1}{2} \ln \left[\frac{E + p_z}{E - p_z} \right] \tag{4.4}$$

where E denotes the particle energy and p_z is the component of the momentum along the beam direction. Since mainly leptons can be considered massless in respect to the nominal centre-of-mass energy, the pseudorapidity, η, is used in stead of using the y. For a massless particle, the *pseudorapidity*, η, depends on the polar angle θ through:

$$\eta = -\ln \tan \frac{\theta}{2} \tag{4.5}$$

For a particle with the energy E much larger than its mass, the approximation $E \approx |\vec{p}|$ is valid. The distance, ΔR, between two objects in the $\eta - \phi$ plan is given by

$$\Delta R = \sqrt{\Delta \eta^2 + \Delta \phi^2} \tag{4.6}$$

where $\Delta \eta$ and $\Delta \phi$ are the difference in pseudorapidity and azimuthal angle, respectively.

4.2.2 The inner detector and tracking system

The *inner detector* (ID) consists of three sub-detectors: the *pixel* detector, the *semi conductor tracker* (SCT), and the *transition radiation tracker* (TRT). The main purpose of the inner detector is to provide high precision measurements of the tracks of particles and to reconstruct the primary and secondary vertices. Each sub-detectors are composed of several layers of material which interacts with the charged particles when the charged particles penetrate the layers. A 2 T magnetic field generated by the central solenoid parallel to the beam axis is applied to bend the charged particles using the Lorentz force. By using the radius r of the curvature of the tracks, the magnetic field strength B, and

the charge of the particle q, we can calculate the magnitude of the transverse momentum p_T:

$$p_T = |q|Br \tag{4.7}$$

The layout of the inner detector is illustrated in Figure 4.3 and the detail of sub-detectors are described in the following paragraphs.
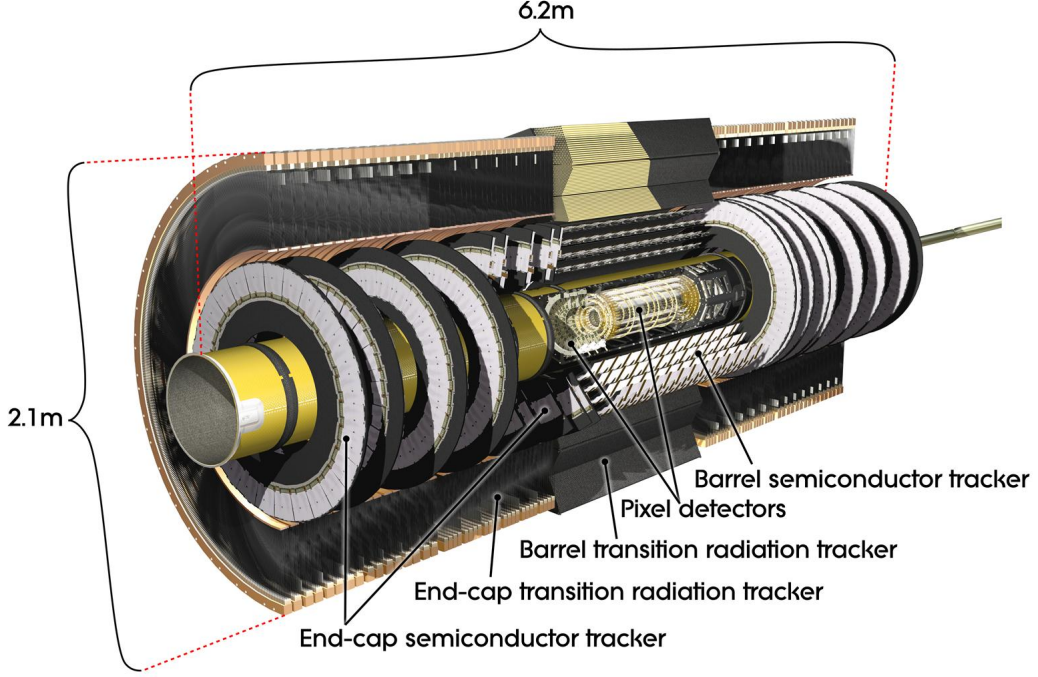
Figure 4.3: Cut-away view of the ATLAS inner detector [2].

Pixel detector

The innermost part of the entire ATLAS detector components is the *pixel* detector which is composed of three barrel layers and three end-cap disks on each side. The three cylindrical barrel layers around the beam axis have radial positions of 50.5 mm, 88.5 mm, and 122.5 mm respectively and they are made of 22, 38, and 52 identical staves respectively. Each stave is inclined with azimuthal angle of 20 degrees and is composed of 13 pixel modules with 46,080 readout channel per module. The size of each pixel is $50 \times 400 \ \mu m^2$

in $R - \phi \times z$. In the forward region, three disks on each side equip the modules identical to the barrel modules, except the connecting cables. The total 1,744 modules in the pixel detector lead to nearly 80 million channel readout and provide the intrinsic accuracies of 10 μm in $R - \phi$ plane and 115 μm in z direction covering the region $|\eta| < 2.5$.

Semi conductor tracker

On the top of the pixel detector is the *semi conductor tracker* (SCT) which is a silicon strip detector. There are about 6.3 million readout channels which are arranged in 4088 microstrips. The intrinsic accuracies per sensor is 17 μm in $R - \phi$ and 580 μm in z direction for the barrel and in R for the disks, respectively. Similar to the pixel detector, the SCT covers the region $|\eta| < 2.5$ and consists of 8 strip layers in barrel and a total of 9 discs in the end-cap region on each side. No track reconstruction is possible beyond the covered pseudorapidity range. Therefore, the electrons cannot be distinguished from photons above $|\eta| > 2.5$ region.

Transition radiation tracker

The outermost component of the inner detector is the *transition radiation tracker* (TRT) which consists of 4 mm diameter straw tubes filled with the xenon-based gas mixture. The gas mixture are ionised by charged particles when they penetrates the straws. The ionised electrons drift to the cathode because a high voltage is applied on the tungsten wire in the center of the straw tube. Therefore, the TRT allows the enhanced electron identification, momentum measurement, vertex measurement. In the barrel region, the straws are surrounded by polypropylene fibres and are divided into two halves at $|\eta| = 0$. In the end-caps, the straws are arranged radially and surrounded by foils as a transition radiation element. They are read out at two sides and at the center of the TRT with the

total number of the readout channels of TRT are approximately 350,000. The TRT only provides information in the $R - \phi$ plane with an intrinsic accuracy of 130 μm per straw and covers a range up to $|\eta| < 2.0$.

Solenoid magnet

A superconducting solenoid magnet encloses the inner detector and produces a 2 T magnetic field to bend the trajectories of the charged particles. A cooling system is used and shared with the *electromagnetic calorimeter* (Section 4.2.3) to reduced the deterioration of the energy measurement.
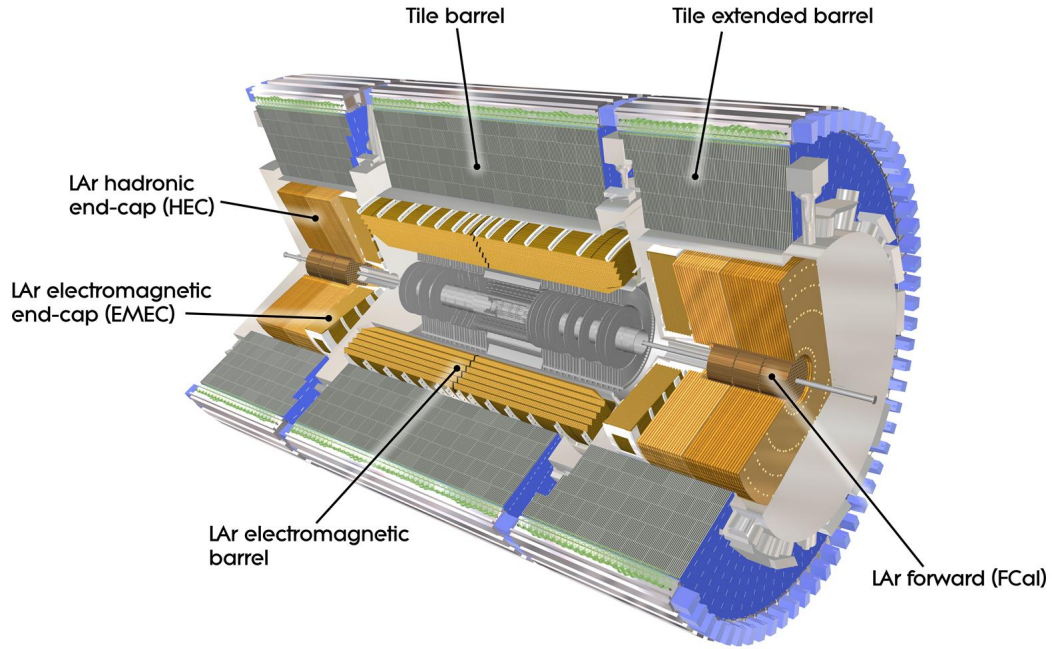
4.2.3   The calorimeters

The calorimeters are used to measure the energy of particles, such as electrons, photons, and jets. Besides muons and neutrinos, all other particles interacting electromagnetically or hadronically are stopped in the calorimeters by absorbing their energy. Not only charged particles but also neutral particles such as photons and neutral hadrons can be detected in the calorimeters. By requiring highly hermiticity of the calorimeters, the missing energy $E_{\mathrm{T}}^{\mathrm{miss}}$ can be reconstructed precisely as negative vectorial sum of all energy deposits. The ATLAS calorimeter system is placed between the inner detector (Section 4.2.2) and the muon spectrometer (Section 4.2.4). The ATLAS calorimeter system consists of an inner *electromagnetic calorimeter* and an outer *hadronic calorimeter* together with the *forward calorimeter*. The electromagnetic calorimeter and hadronic calorimeter are *sampling calorimeters* which consist of two different materials alternately. An absorber material is used to enhance the particle showers[7] and a highly ionisable active

---

[7]The shower is the cascade of secondary particles produced by the high-energy particle interacting with dense material.

medium is used to measure the deposited energy. Because only the energies deposited in the active medium can be observed, the total energy of the shower can be estimated from the deposited energy by clustering algorithms. The electromagnetic calorimeter is focusing on measuring electrons and photons, and the hadronic calorimeter is dedicated for hadronically interacting particles. The whole ATLAS calorimeter system covers a range $|\eta| < 4.9$. An layout view of the ATLAS calorimeter system is shown in Figure 4.4 and the detail of the three calorimeters are described in the following paragraphs.

Figure 4.4: Cut-away view of the calorimeter system [2].

Electromagnetic calorimeter

The *electromagnetic calorimeter* (ECAL) measures the energy of electrons and photons as they interact with matter. The ECAL consists of accordion shaped cells of alternating layers of lead as absorber material and liquid argon (LAr) as active medium. The accordion shaped provides the full coverage in the azimuthal angle ϕ. The LAr is chosen as an active

medium because it is hard to radiate, it has stable response time and linear behaviour [2]. The electrons or photons lose their energies by alternating bremsstrahlung and pair production when they interact with lead and result in the electromagnetic particle showers which ionise the LAr and the ionisation currents are collected by the copper electrodes. The ECAL is divided into barrel (EMB) and end-cap (EMEC) components, which cover $|\eta| < 1.475$ and $1.375 < |\eta| < 3.2$[8], respectively. The EMB is made up of three longitudinal layers with different granularity and sensitive in the region $|\eta| < 2.5$. The first strip layer has the highest granularity where the size of cells corresponding to $\Delta\eta \times \Delta\phi = 0.0031 \times 0.1$ for $|\eta| < 1.8$ and coarser for larger $|\eta|$. The smallest granularity allows to separate the showers coming from electrons, photons and neutral pions. The second layer is the largest part of the EMB with the size of cells corresponding to $\Delta\eta \times \Delta\phi = 0.025 \times 0.0245$ so most of the energies are deposited in this layer. The third layer has the granularity $\Delta\eta \times \Delta\phi = 0.05 \times 0.0245$. The total thickness are 22 X_0[9] and 24 X_0 for EMB and EMECs, respectively. This special thickness is sufficient to prevent the punch-throughs of high energy showers into the muon spectrometer. Figure 4.5 shows the cut-away view of the the accordion shaped EMB module with the dimensions for three layers.

Hadronic calorimeter

The electromagnetic interacting particles produce narrow showers, however, the hadrons, which are heavier and penetrate medium further, produce more wide-spread hadronic showers. The *hadronic calorimeter* (HCAL) surrounds the ECAL and is made up by a barrel and two end-caps (HEC). The barrel covers $|\eta| < 1.7$ and it uses plastic scintillator tiles as active medium and steel as absorber material. The hadronic showers stimulate

---

[8]There are two EMECs and each of them consists of two wheels. The inner wheel covers $1.375 < |\eta| < 2.5$ and the outer wheel covers $2.5 < |\eta| < 3.2$

[9]The X_0 stands for radiation lengths which is a characteristic of material. It is related to the energy loss of the particle when it interacts with the material electromagnetically.
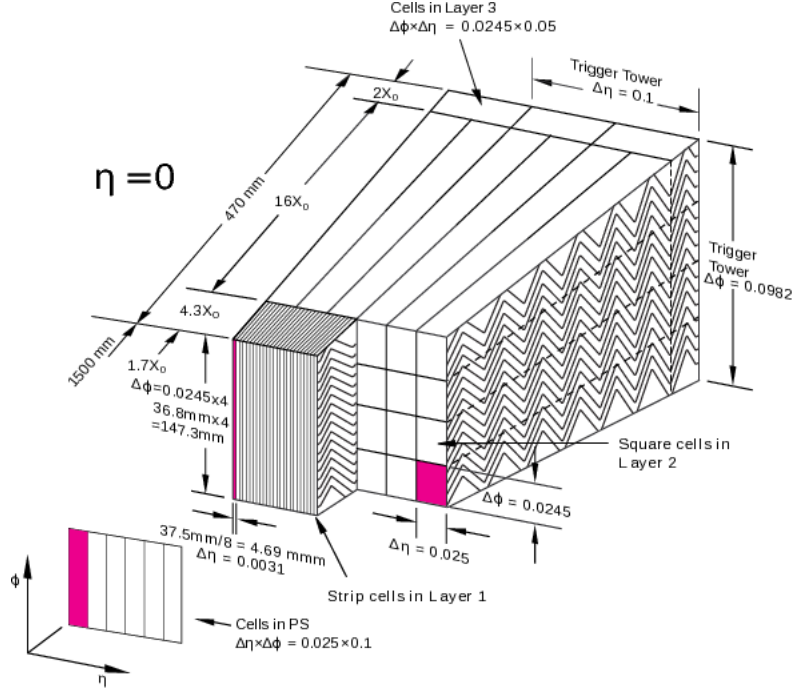
Figure 4.5: Cut-away view of the accordion shaped EMB module with the dimensions for three layers [8].

the scintillator and emit light which is collected by *photo multiplier tubes* (PMTs) and then read-out via wavelength shifting optical fibers. The HEC covers $1.5 < |\eta| < 3.2$ which overlap with the pseudorapidity coverage region of barrel. The HEC is composed of two copper plate wheels as absorber material on each side and the LAr in between. The designed thickness in the barrel region is 9.7 λ[10]. Therefore, the punch-through to the muon spectrometer is suppressed. The granularity of the HCAL is coarser than the ECAL but it is sufficient for measuring E_T^{miss} and jet reconstruction.

Forward calorimeter

The *forward calorimeter* (FCAL) uses the LAr as active medium and one copper and two tungsten layers as absorber materials. The copper layer (FCAL1) is used to measure

---

[10]The λ represents the hadronic interaction lengths which is the mean free path of a strongly interacting particle between two inelastic scatterings.

the electromagnetic interactions whereas the two tungsten layers (FCAL2 and FCAL3) is used to measure the hadronically interactions. The FCAL provides the very forward region coverage $3.1 < |\eta| < 4.9$ can contribute the $E_{\mathrm{T}}^{\mathrm{miss}}$ measurement.

Energy resolution

The energy resolution is the ability of the calorimeter to distinguish the two adjacent energies. The number of ionized particles N is proportion to the energy E of the incoming particle. Therefore, the higher energy of the incoming particle the more inoized particles produced in the shower. Based on the Poisson statistics we know

$$\frac{\sigma_E}{E} \propto \frac{\sigma_N}{N} = \frac{\sqrt{N}}{N} = \frac{1}{\sqrt{N}} \propto \frac{1}{\sqrt{E}} \tag{4.8}$$

where σ_E is the energy resolution at FWHM[11] in a Gaussian distribution and $\sigma_N = \sqrt{N}$ is the Poisson standard deviation. Taking the effects of calibration and electronics noise into account, the relative energy resolution becomes

$$\frac{\sigma_E}{E} = \frac{a}{E} \oplus \frac{b}{\sqrt{E}} \oplus c \tag{4.9}$$

where a, b, c are noise, sampling, and constant terms, respectively. The relative energy resolutions for ECAL, HCAL, and FCAL are summarised in Table 4.1.

Calorimeter	Required resolution
Electromagnetic calorimeter	$\sigma_E/E = 10\%/\sqrt{E(\mathrm{GeV})} \oplus 0.7\%$
Hadronic calorimeter	$\sigma_E/E = 50\%/\sqrt{E\ (\mathrm{GeV})} \oplus 3\%$
Forward calorimeter	$\sigma_E/E = 100\%/\sqrt{E\ (\mathrm{GeV})} \oplus 10\%$

Table 4.1: Resolution requirements for the different calorimeters of the ATLAS detector [2].

---

[11]The FWHM means full width at half maximum.

4.2.4 The muon spectrometer

The outermost part of the ATLAS detector is the *muon spectrometer* [2, 43, 44]. Muons have the same properties as electrons but 200 times heavier than the electrons. Because muons don't interact predominately by bremsstrahlung, most of the muons escape the inner detector and calorimeters without being stopped. Only the muons with an energy less than 5 GeV are stopped before the muon spectrometer. Therefore, a detector concentrates on the measurement of high precision momentum and trajectory of muons is necessary.

The muon spectrometer is designed to measure the transverse momentum (p_T) of muons with $p_T > 3$ GeV with a resolution of 3% for $p_T < 250$ GeV and increasing to 10% at 1 TeV. It consists of large toroid magnets system and high precision tracking chambers allowing a precise measurement of the muon momentum over nearly the full solid angle. The barrel toroid magnet system is composed of eight superconducting coils which are installed radial symmetrically around the beam pipe. It covers the range $|\eta| < 1.4$ and bends the trajectories of muons with the bending power 1.5 to 5.5 Tm. The magnetic field produced by the barrel toroid magnets provides an approximately 1 T field at the center of each coils, but is rather non-uniform, especially in the barrel-endcap transition region. In the endcap toroid magnets system, the magnetic field is provided by eight superconducting coils, closed in an insulation vessel extending to about 10 m in diameter, located between the first and the second station of tracking chambers. The endcap toroid magnets cover $1.6 < |\eta| < 2.4$ and provide a magnetic field in the range of 1 to 2 T with bending power 1 to 7.5 Tm.

The *monitored drift tubes* (MDT) consists of cylindrical drift tubes, filled with a gas mixture of Ar and CO_2. A tungsten-rhenium alloyed aluminium wire in the centre of each tube collects the electrons freed by ionisation of the gas volume by traversing muons. The

MDT covers a full range of $|\eta| < 2.7$, while the inner layer only covers $|\eta| < 2.0$. The *cathode strip chambers* (CSC) provides a coverage range $2.0 < |\eta| < 2.7$, where MDTs would have occupancy problems. The CSC is made up by two discs and filled with Ar and CO_2 gas mixture. Both MDT and CSC are slow for trigger but they provide high precision tracking in the spectrometer bending plane and end-cap inner layer, respectively. The *resistive plate chambers* (RPC) and *thin gap chambers* (TGC) are used for triggering in barrel and end-cap, they have sufficient intrinsic time resolution of 1.5 ns and 4 ns, respectively. A sketch of the muon spectrometer and its four components are depicted in Figure 4.6 and Table 4.2 gives a summary of the muon spectrometer components
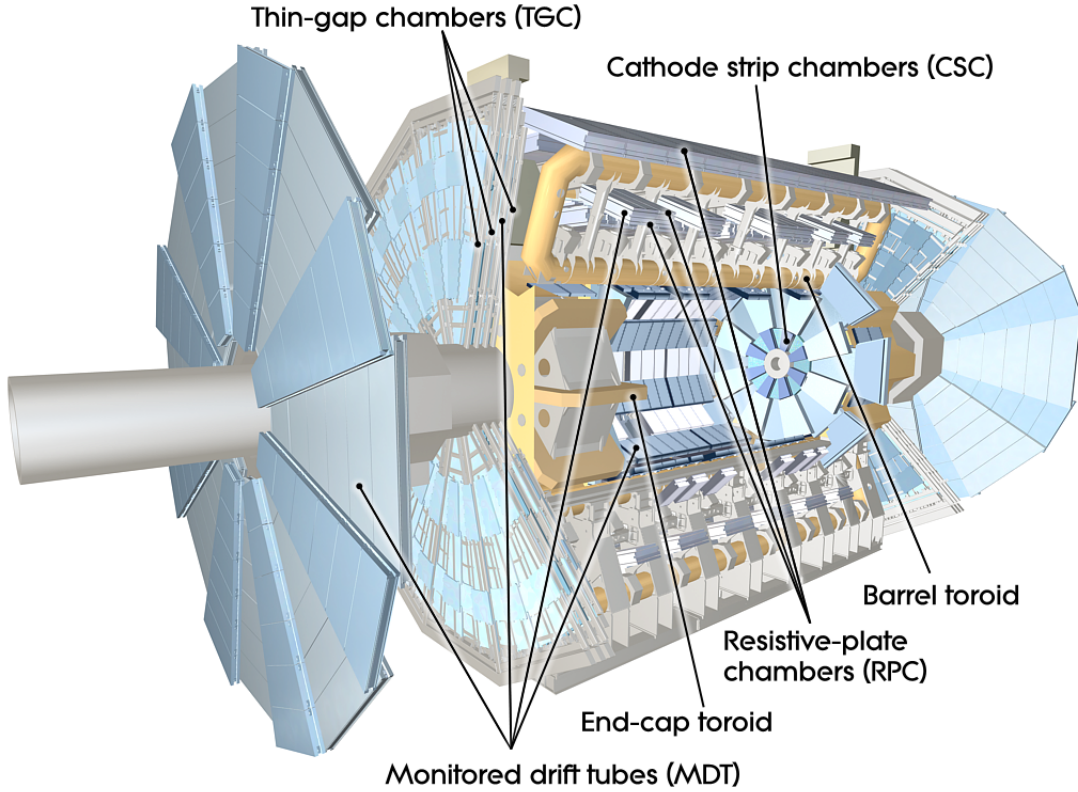
Figure 4.6: Sketch of the muon system of the ATLAS detector [2].

Type	Purpose	Location	η coverage	Channel
MDT	Tracking	barrel + end-cap	$0.0 < \eta < 2.7$	354k
CSC	Tracking	end-cap layer 1	$2.0 < \eta < 2.7$	30.7k
RPC	Trigger	barrel	$0.0 < \eta < 1.0$	373k
TGC	Trigger	end-cap	$1.0 < \eta < 2.4$	318k

Table 4.2: A summary of the muon spectrometer components.

4.2.5 The trigger system and data acquisition

The LHC pp collision rate is 40 MHz corresponding to 50 TB/s data[12] generated by the ATLAS detector [45]. However, the limited rate for writing the events into disk is about 1 kHz[13]. The majority of the products of the pp collision are low p_T QCD processes which are not the interesting events for the analysis. Hence, the three-level ATLAS trigger and data acquisition (DAQ) system is designed to pick the interesting events and reduce the data size. Figure 4.7 shows the functional view of the ATLAS trigger/DAQ system and the brief descriptions are given in the following paragraph.

The level-1 trigger

The initial selection is made by the hardware-based *level-1* (LVL1) trigger based on reduced-granularity information from calorimeters and the muon spectrometer. The latency[14] of the level-1 trigger is required to be less than 2.5 μs[15]. The high p_T muons are identified using only RPC and TGC. The high p_T e/γ, jets, hadronically decaying

---

[12]Assuming the typical event size is 1.3 MB.

[13]The data storage rate is 200 Hz in Run-1 but it is increased to about 1 kHz in Run-2.

[14]The latency is the time interval from the pp collision until trigger decision is available to the front-end electronics.

[15]The target latency for the level-1 trigger is 2.0 μs
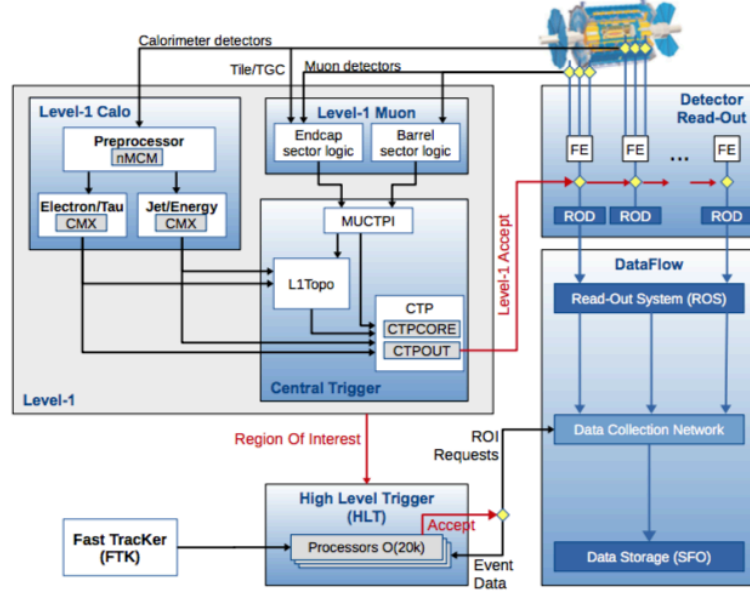
Figure 4.7: The schematic view of the ATLAS trigger/DAQ system in Run-2. The figure is taken from [9]

τ-leptons, large $E_{\mathrm{T}}^{\mathrm{miss}}$ and total E_{T} objects are selected by calorimeter trigger using a number of sets of p_{T} thresholds[16] and the energy isolation cuts can be applied. The selected events are read out from the front-end electronics into *readout drivers* (RODs) and written into *readout buffers* (ROBs). The information such as the p_{T}, η, and ϕ of the candidate objects and $E_{\mathrm{T}}^{\mathrm{miss}}$ and total E_{T} are saved into *region-of-interest* (ROI) and send to the high level trigger. The level-1 trigger reduces the event rate from the high LHC bunch crossing rate to 100 kHz.

The high level trigger

The *level-2* trigger and *event filter* (EF) computer clusters used in Run-1 are merged into a single event professing *high level trigger* (HLT) farm in Run-2. This combination reduces the complexity, allows resource sharing between algorithms, and results in a more

---

[16]Typically, there are 6 to 8 sets of thresholds per object type.

flexible HLT. The HLT is completely software based trigger system and it uses the ROI information from the level-1 trigger and the tracking information from the inner detector. The full-event track reconstruction information is performed by the *fast tracker* (FTK) system after each level-1 trigger and provided to the HLT. The trigger reconstruction algorithms for HLT were re-optimised to minimise the differences between the HLT and the offline analysis selections. The output rate of the HLT is approximately 1 kHz within a processing time about 200 μs.

References

[1] K.A. Olive et al (Particle Data Group). Review of particle physics. *Chin. Phys. C*, 38(9):090001, 2014. (document), 2.1, 2.1.1

[2] The ATLAS Collaboration. The atlas experiment at the cern large hadron collider. *Journal of Instrumentation*, 3(08):S08003, 2008. (document), 4, 4.2, 4.2, 4.3, 4.4, 4.2.3, 4.1, 4.2.4, 4.6

[3] John Ellis. Higgs physics. *arXiv*, arXiv:1312.5672v1, 2015. (document), 2.1

[4] ATLAS Collaboration. Observation of a new particle in the search for the standard model higgs boson with the atlas detector at the lhc. *Phys. Lett. B*, 716(1):1–29, Sept 2012. (document), 2.1.5, 2.2

[5] CMS Collaboration. Observation of a new boson at a mass of 125 gev with the cms experiment at the lhc. *Phys. Lett. B*, 716(1):30–61, Sept 2012. (document), 2.1.5, 2.2

[6] (document), 2.3

[7] Fabienne Marcastel. Cern's accelerator complex. la chaîne des accélérateurs du cern. *OPEN-PHO-CHART-2013-001*, Oct 2013. (document), 4.1

[8] Nikiforos Nikiforou. Performance of the atlas liquid argon calorimeter after three years of lhc operation and plans for a future upgrade. *arXiv*, arXiv:1306.6756v2, Jun 2013. (document), 4.5

[9] The ATLAS Collaboration. The run-2 atlas trigger system. *J. Phys. Conf. Ser.*, 762(1):012003, Feb 2016. (document), 4.7

[10] Abdus Salam and J.C. Ward. Weak and electromagnetic interactions. *Nuovo Cimento*, 11(4):568–577, Feb 1959. 2, 2.1.4

[11] Sheldon L. Glashow. Partial-symmetries of weak interactions. *Nuclear Physics*, 22(4):579–588, Feb 1961. 2, 2.1.4

[12] Steven Weinberg. A model of leptons. *Phys. Rev. Lett.*, 19(21):1264–1266, Nov 1967. 2, 2.1.4

[13] M. Herrero. The standard model. *NATO Sci. Ser. C*, 534:1–59, 1999. 2

[14] D. A. Greenwood W. N. Cottingham. *An Introduction to the Standard Model of Particle Physics*. Cambridge University Press, 2 edition, 2007. 2

[15] Emmy Noether. Invariant variation problems. *Transport Theory and Statistical Physics*, 1(3):186–207, 1971. 2.1

[16] E. Fermi. Versuch einer theorie der -strahlen. i. *Zeitschrift für Physik*, 88(3-4):161–177, Mar 1934. 2.1.4

[17] Tadao Nakano and Kazuhiko Nishijima. Charge independence for v-particles. *Progress of Theoretical Physics*, 10(5):581–582, 1953. 2.1.4

[18] M. Gell-Mann. The interpretation of the new particles as displaced charge multiplets. *Nuovo Cim*, 4(2):848–866, Apr 1956. 2.1.4

[19] Makoto Kobayashi and Toshihide Maskawa. Cp-violation in the renormalizable theory of weak interaction. *Progress of Theoretical Physics*, 49(2):652–657, Feb 1973. 2.1.4

[20] Ziro Maki, Masami Nakagawa, and Shoichi Sakata. Remarks on the unified model of elementary particles. *Progress of Theoretical Physics*, 28(5):870–880, Nov 1962. 2.1.4

[21] Peter W. Higgs. Spontaneous symmetry breakdown without massless bosons. *Phys. Rev.*, 145(4):1156–1163, May 1964. 2.1.4

[22] Peter W. Higgs. Broken symmetries and the masses of gauge bosons. *Phys. Rev. Lett.*, 13(16):508–509, Oct 1964. 2.1.4

[23] Peter W. Higgs. Broken symmetries, massless particles and gauge fields. *Physics Letters*, 12(2):132–133, Sept 1964. 2.1.4

[24] F. Englert and R. Brout. Broken symmetry and the mass of gauge vector mesons. *Phys. Rev. Lett.*, 13(9):321–323, Aug 1964. 2.1.4

[25] G. S. Guralnik, C. R. Hagen, and T. W. B. Kibble. Global conservation laws and massless particles. *Phys. Rev. Lett.*, 13(20):585–587, Nov 1964. 2.1.4

[26] Stephen P. Martin. A supersymmetry primer. *arXiv*, hep-ph/9709356, 1997. 2.2.1

[27] Piotr H. Chankowskia, John Ellisb, Keith A.Olivec, and Stefan Pokorskia. Cosmological fine tuning, supersymmetry and the gauge hierarchy problem. *Physics Letters B*, 452(1-2):28–38, Apr 1999. 2.2.1

[28] Maarten C. Brak. The hierarchy problem in the standard model and little higgs theories. Oct 2004. 2.2.1

[29] WMAP Collaboration. Nine-year wilkinson microwave anisotropy probe (wmap) observations: Final maps and results. *arXiv*, arXiv:1212.5225v3 [astro-ph.CO], 2012. 2.2.2

[30] P. A. R. Ade et al. Planck 2013 results. i. overview of products and scientific results. *Astron. Astrophys.*, 571, 2014. 2.2.2

[31] Gianfranco Bertone, Dan Hooper, and Joseph Silk. Particle dark matter: evidence, candidates and constraints. *Physics Reports*, 405(5-6):279–390, 2005. 2.2.2

[32] G. Ross. Grand unified theories: Frontiers in physics. *Physics Bulletin*, 37(10):429, 1986. 2.2.3

[33] Peter J. Mohr, Barry N. Taylor, and David B. Newell. Codata recommended values of the fundamental physical constants: 2010. *Rev. Mod. Phys.*, 84(4):1527–1605, Nov 2012. 2.2.3

[34] Lyndon Evans and Philip Bryant. Lhc machine. *Journal of Instrumentation*, 3(08):S08001, 2008. 4, 4.1, 4.2

[35] The CMS Collaboration. The cms experiment at the cern lhc. *Journal of Instrumentation*, 3(08):S08004, 2008. 4

[36] The ALICE Collaboration. The alice experiment at the cern lhc. *Journal of Instrumentation*, 3(08):S08002, 2008. 4

[37] The LHCb Collaboration. The lhcb detector at the lhc. *Journal of Instrumentation*, 3(08):S08005, 2008. 4

[38] The TOTEM Collaboration. The totem experiment at the cern large hadron collider. *Journal of Instrumentation*, 3(08):S08007, 2008. 4

[39] The LHCf Collaboration. The lhcf detector at the cern large hadron collider. *Journal of Instrumentation*, 3(08):S08006, 2008. 4

[40] James Pinfold, R Soluk, Y Yao, S Cecchini, G Giacomelli, M Giorgini, L Patrizii, G Sirri, D H Lacarrère, K Kinoshita, J Jakubek, M Platkevic, S Pospísil, Z Vykydal, T Hott, A Houdayer, Claude Leroy, J Swain, D Felea, D Hasegan, G E Pavalas, and V" Popa. Technical design report of the moedal experiment. *CERN-LHCC-2009-006*, CERN-LHCC-2009-006(MoEDAL-TDR-001), Jun 2009. 4

[41] L. Rossi. The lhc superconducting magnets. In *Proceedings of the 2003 Particle Accelerator Conference*, volume 1, pages 141–145 Vol.1, May 2003. 4.1

[42] The lhc sees its first circulating beam. 4.1

[43] S Palestini. The muon spectrometer of the atlas experiment. Technical Report ATL-MUON-2004-001, CERN, Geneva, Feb 2003. Contribution to the proceedings : 8th Topical Seminar on Innovative Particle and Radiation Detectors, 21-24 Oct. 2002, Siena, Italy. 4.2.4

[44] ATLAS muon collaboration. Atlas muon detector commissioning. *arXiv*, arXiv:0910.2767v1, 2009. 4.2.4

[45] The ATLAS Collaboration. The atlas data acquisition and trigger: concept, design and status. *Nucl. Phys. B Proc. Suppl.*, 172:178–182, Oct 2007. 4.2.5